Controlled preparation of $Gd_2O_2SO_4:Eu^{3+}$ monospheres via hydrothermal precursor engineering for enhanced photoluminescence

Fan Li,[a] Sihan Feng,[a] Zhiyuan Pan,[a] Qi Zhu,[a] Xudong Sun,[a] Ji-Guang Li[b,*]

[a] *Key Laboratory for Anisotropy and Texture of Materials (Ministry of Education), School of Materials Science and Engineering, Northeastern University, Shenyang, Liaoning 110819, China*

[b] *Research Center for Electronic and Optical Materials, National Institute for Materials Science, Tsukuba, Ibaraki 305-0044, Japan*

[*]Corresponding author

Dr. Ji-Guang Li

National Institute for Materials Science

Tel: +81-29-860-4394

E-mail: li.jiguang@nims.go.jp

Abstract

Rare-earth oxysulfate ($RE_2O_2SO_4$) attracted attention for large-capacity oxygen storage, low-temperature magnetism and luminescence, whose preparation mostly involves toxic SO_x gases and/or complicated procedures. In the phosphor field, monospheres are preferred for a number of applications due to their better luminescence and high packing density. With the simple reactants of $RE(NO_3)_3$, Na_2CO_3 and $(NH_4)_2SO_4$ for hydrothermal reaction, dispersed monospheres and nanoplates were selectively synthesized for the recently discovered $RE_2(OH)_2CO_3SO_4 \cdot nH_2O$ (RE = $Gd_{0.95}Eu_{0.05}$, REOCSH) layered compound precursor, from which $RE_2O_2SO_4$ phosphors mostly retaining their precursor morphologies were facilely derived via calcination in air at 800 °C, without involving SO_x. Solution pH was found to decisively determine the chemical composition and crystallization kinetics of the initial precipitate, and the possible mechanisms of phase/morphology evolution during hydrothermal treatment were proposed by comparatively investigating the temperature-course and time-course of REOCSH formation under the typical pH values of 6 and 7. It was revealed that $(Gd_{0.95}Eu_{0.05})_2O_2SO_4$ monospheres emit ~1.35 times as strong as nanoplates (λ_{ex} = 257 nm, λ_{em} = 617 nm) and may retain as high as ~81% of the room-temperature intensity at 150 °C. The phosphor monospheres were also analyzed to have a fluorescence lifetime of ~1.32 ms at room temperature and an activation energy of ~0.19 eV for the thermal quenching of luminescence.

***Keywords**:* $RE_2O_2SO_4$; Luminescence; Hydrothermal reaction; Phase/morphology evolution

1. Introduction

Rare-earth oxysulfates ($RE_2O_2SO_4$) attracted attention due to their large capacity of oxygen storage (RE = La, Pr, Nd, Sm) [1, 2] and unusual low-temperature magnetism (RE = Gd, Tb, Dy, Ho, Er, Tm) [3-5]. Recent studies also showed that they are promising hosts for luminescence applications (RE = La, Gd, Y) [6-9]. The family of compounds all have a layered crystal structure in the monoclinic system (Space group *C*2/*c*), which is formed by alternative stacking of $[RE_2O_2]^{2+}$ main layers and inter-layer $[SO_4]^{2-}$ along the *a*-axis [10, 11], as shown in Fig. S1 with $La_2O_2SO_4$ [10] for example. In such a structure, two opposite O atoms of each $[SO_4]^{2-}$ tetrahedron are respectively coordinated with two RE in neighboring $[RE_2O_2]^{2+}$ layers [10, 11]. The physicochemical properties of a material are known to be susceptible to morphology, geometric dimension and surface chemistry [12-14]. Therefore, shape-controlled synthesis of multi-dimensional materials is of great significance for novel/enhanced functionalities [12, 15, 16]. For instance, two-dimensional (2D) materials are attractive for application in catalysis and sensors due to their better electron transport properties arising from a large specific surface area and unsaturated surface [17, 18]. Spherical particles, on the other hand, are preferred for luminescence in the field of lighting and display, since a dense phosphor layer may be formed via close packing of the spheres, and such a morphology may minimize surface scattering of the excitation/emission light.

Thermal decomposition of $RE_2(SO_4)_3{\cdot}nH_2O$ is the common method for $RE_2O_2SO_4$ preparation. While simple to operate, it is not conducive to morphology control and, particularly, releases toxic SO_x gases [1, 19]. To this end, scholars made efforts to develop alternative synthesis techniques, mostly based on liquid-phase processing. For example, with a precursor

formed by RE^{3+} and dodecyl sulfate ($C_{12}H_{25}OSO_3^-$, DS^-), Machida et al. [20, 21] obtained ~10 nm sized $La_2O_2SO_4$ and $Pr_2O_2SO_4$ crystallites by subsequent calcination at 900 °C. Qu et al. [22] obtained $Y_2O_2SO_4$ nanofibers with an average diameter of ~90 nm through annealing the precursor fibers produced by electrospinning a solution of $Y(NO_3)_3{\cdot}6H_2O$, thiourea (H_2NCSNH_2) and polyvinylpyrrolidone (PVP). Liu et al. [6] prepared $Y_2O_2SO_4$:Eu^{3+} hollow spheres of ~1 μm by calcining at 650 °C a precursor obtained by a L-cysteine/PVP assisted hydrothermal method and studied their photoluminescence. Wang et al., on the other hand, obtained $RE_2O_2SO_4$ for the full range of lanthanide elements and Y by calcining in air the $RE_2(OH)_4SO_4{\cdot}nH_2O$ layered hydroxides (SO_4^{2-}-LRH; n = 0 or 2 depending on the type of RE) synthesized via hydrothermal reaction, and the RE-dependent occurrence of $RE_2O_2SO_4$ was revealed via thermal analysis [23-25]. In our efforts to synthesize $Gd_2(OH)_4SO_4{\cdot}nH_2O$ via hydrothermal reaction of Gd nitrate, ammonium sulfate (SO_4^{2-} source) and urea (OH^- and CO_3^{2-} source) at 140 °C, $Gd_2(OH)_2CO_3SO_4{\cdot}nH_2O$ was discovered as a new type of layered compound, which transforms to $Gd_2O_2SO_4$ via dehydroxylation and decarbonation. While such a reaction system allowed to build aligned films through heterogenous nucleation and homogeneous precipitation, pH control appeared as a problem owing to the uncertainties arising from urea hydrolysis ($CO(NH_2)_2 + H_2O \rightarrow NH_3{\cdot}H_2O + CO_3^{2-}$). This also prevented us from mechanism understanding of $Gd_2(OH)_2CO_3SO_4{\cdot}nH_2O$ formation and morphology control of the product. We thus replaced urea with sodium carbonate as the CO_3^{2-} source for $Gd_2(OH)_2CO_3SO_4{\cdot}nH_2O$ (doped with Eu^{3+}) synthesis in this work, which produced uniformly dispersed nanoflakes and microspheres as two types of distinctly different products. The temperature-course and time-course of phase and morphology evolution were revealed by

regulating solution pH, and the derived $Gd_2O_2SO_4:Eu^{3+}$ phosphors were comparatively studied for photoluminescence. It was shown that the $Gd_2O_2SO_4:Eu^{3+}$ microspheres have a significantly better performance and may serve as a red phosphor with good thermal stability.

2. Experimental Section

2.1. Hydrothermal synthesis

The synthesis of $RE_2(OH)_2CO_3SO_4 \cdot nH_2O$ (RE = $Gd_{0.95}Eu_{0.05}$) was conducted via hydrothermal reaction of RE nitrate, $(NH_4)_2SO_4$ (analytical grade, Sinopharm Co., Ltd., Shanghai, China) and Na_2CO_3 (analytical grade, Sinopharm), where the RE nitrate was prepared by dissolving Gd_2O_3 and Eu_2O_3 (99.99% pure, Huizhou Co., Ltd.) with a proper amount of nitric acid (analytical grade, Sinopharm). Ultra-pure water (resistivity > 18 MΩ·cm) was used throughout the experiments. In a typical synthesis, 1.5 mmol of $(NH_4)_2SO_4$ and 1.5 mmol of Na_2CO_3 were dissolved in a certain amount of water to make a transparent solution, to which 3 mmol of RE nitrate ($RE^{3+}:SO_4^{2-}:CO_3^{2-}$ = 2:1:1 molar ratio) was added under magnetic stirring, followed by pH adjustment to a designated value (6.0-10) with NH_4OH and/or HNO_3 while keeping the total volume at 60 mL. The resultant mixture was constantly stirred for 30 min before being transferred into a Teflon lined stainless steel autoclave (100 mL capacity) for 24 h of reaction in an electric oven preheated at a predetermined temperature (100-200 °C). After the reaction, the precipitate was collected via centrifugation, washed with water and ethanol successively, and then dried at 60 °C for 12 h to yield a white precursor powder. $(Gd_{0.95}Eu_{0.05})_2O_2SO_4$ was produced by calcining the precursor in stagnant air at 800 °C for 1 h, using a heating rate of 8 °C/min at the ramp stage. In this work, the content of Eu^{3+} was taken as the optimal value of 5 at.% according to a previous report on $La_2O_2SO_4:Eu^{3+}$ [26].

2.2. Characterization

Phase identification was performed via X-ray diffractometry (XRD, SmartLab, Rigaku, Tokyo, Japan) under 40 kV/200 mA, using nickel-filtered Cu-Kα radiation (λ= 0.15406 nm) and a scanning speed of 4°/min for 2θ. Product morphology was analyzed by field emission scanning electron microscopy (FE-SEM, Model JSM-7001F, JEOL, Tokyo) under an acceleration voltage of 15 kV. Fourier transform infrared spectroscopy (FTIR, Nicolet iS5, Thermo Fisher Scientific, Waltham, USA) was conducted using the standard KBr pellet method. Photoluminescence and fluorescence decay were analyzed with a Model FP-8600 fluorospectrophotometer (JASCO, Tokyo) that is equipped with a 60 mm-diameter integrating sphere and a Model HPC-836 temperature controller (JASCO), using a 150 W xenon lamp for excitation, a scan speed of 100 nm/min, and a slit width of 5 nm.

3. Results and discussion

3.1 The effect of solution pH on phase and morphology evolution of $RE_2(OH)_2CO_3SO_4 \cdot nH_2O$

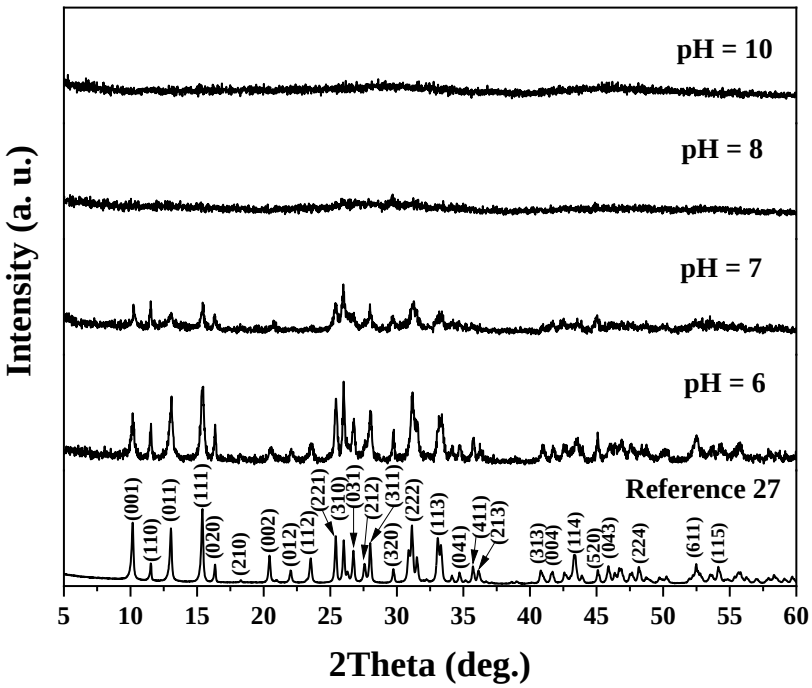

Fig. 1. XRD patterns of the products obtained at different solution pH, where the diffraction of $Gd_2(OH)_2CO_3SO_4 \cdot nH_2O$ (n ~ 1.0) [27] was included for comparison.

The reaction system before hydrothermal treatment has been turbid, and reaction at 140 °C for 24 h produced a white precipitate in each case. XRD analysis (Fig. 1) found that solution pH has a pronounced effect on the hydrothermal product, and crystalline $RE_2(OH)_2CO_3SO_4{\cdot}nH_2O$ (REOCSH; RE = $Gd_{0.95}Eu_{0.05}$) can only be obtained under pH = 6 and 7, though the pH = 6 product was much better crystallized. FE-SEM analysis (Fig. 2) demonstrated that the pH = 6 sample crystallized as discrete nanoflakes with edge lengths of up to ~400 nm (Fig. 2a and the inset) and the pH = 7 sample consists of monodisperse microspheres of up to ~25 μm in diameter (average size ~17 μm; Fig. 2b). Closer view showed that each of the monospheres has a rough surface and was formed by face-to-face vertical stacking of nanoflakes (edge length ~600 nm and thickness ~35 nm; the inset in Fig. 2b). Though similarly amorphous, the pH = 8 product mostly contains ~50 μm-sized spheres (Fig. 2c) while the pH =10 one is composed of irregular-shaped aggregates (Fig. 2d). In both the latter cases, however, the primary building units are rounded nanoparticles of ~30 nm, as revealed by high magnification FE-SEM observation (the insets in Fig. 2c,d). The results thus imply that crystallization was accompanied by fast 2D development of the crystallites owing to the tetragonal crystal structure of REOCSH.

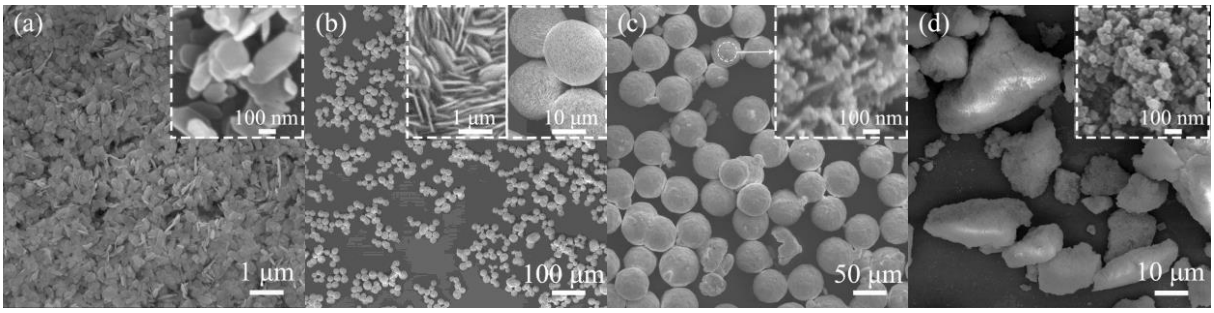

Fig. 2. FE-SEM morphologies of the products obtained at pH = 6 (a), 7 (b), 8 (c) and 10 (d). The insets are closer views.

To clarify the chemical species contained in the hydrothermal products, especially the

amorphous ones, FTIR analysis was performed for the series of samples and the results are shown in Fig. 3. It was found that all the products share similar vibrational absorptions, which are generated by OH^- at ~3553 cm^{-1} (O–H stretching, ν_1), H_2O at ~3420 cm^{-1} (O–H stretching, ν_1)/1645 cm^{-1} (H–O–H bending, ν_2), CO_3^{2-} at ~842 cm^{-1} (ν_2, weak) and in the regions of ~1300-1590 cm^{-1} (ν_3, strong)/670-808 cm^{-1} (ν_4, medium strong), and SO_4^{2-} at ~1010/991 cm^{-1} (ν_1)/600 cm^{-1} (ν_4) and in the regions of ~1025-1270 cm^{-1} (ν_3) [28, 29]. Compared with the amorphous products (pH = 8 and 10), the crystalline ones showed sharper and significantly more split SO_4^{2-} and CO_3^{2-} bands, implying that these two kinds of ligands are more tightly coordinated to the RE^{3+} center ions. Though the chemical species are the same, the content of each differs for the crystalline and amorphous products, since the pH = 10 sample turned into a phase mixture (Fig. S2) of monoclinic $Gd_2O_2SO_4$ (ICDD No. 04-024-9775) and cubic Gd_2O_3 (~73 wt%; ICDD No. 12-0797) while the pH = 6 and 7 ones turned into pure $Gd_2O_2SO_4$ (shown later) by calcination at 800 °C. In view that REOCSH has exactly the same RE^{3+}/SO_4^{2-} molar ratio of $RE_2O_2SO_4$, the appearance of RE_2O_3 indicates that the pH = 10 sample has an off-stoichiometric amount of SO_4^{2-} when compared with REOCSH.

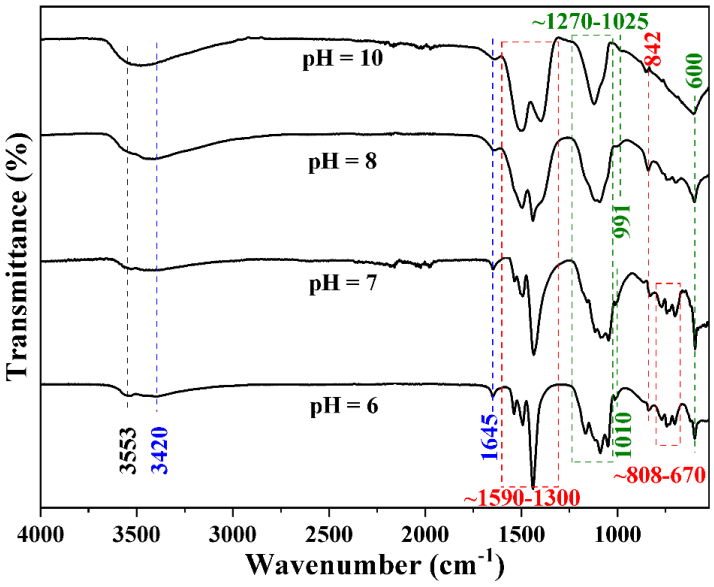

Fig. 3. FTIR spectra of the hydrothermal products obtained at the different pH values.

To understand the effect of solution pH on crystallization and phase formation, the precipitate recovered from the reaction system before hydrothermal treatment was subjected to XRD analysis. As shown in Fig. S3, all the initial precipitates are similarly amorphous irrespective of solution pH. For a better understanding, the amorphous precipitates were calcined in air at 800 °C for 1 h, and XRD analysis indicated that the calcination products are a phase mixture of $RE_2O_2SO_4$ and RE_2O_3 in each case (Fig. 4). Rietveld refinement of the XRD patterns with software Jade 7.1 further revealed that the fraction of RE_2O_3 significantly increases with increasing solution pH, being ~18.7, 25, 68.5 and 75 wt% for pH = 6, 7, 8 and 10, respectively. This implies that a gradually less amount of SO_4^{2-} was incorporated into the amorphous precipitate at a higher solution pH. Such a result can be understood by considering the solution chemistry of RE^{3+} and the chemical species existing in the reaction system. In this work, RE^{3+} would exist as $[RE(OH)_a(CO_3)_b(SO_4)_c(H_2O)_d]^{3-a-2b-2c}$ complex ion, where the OH^-, CO_3^{2-}, SO_4^{2-} species are expected to compete with each other to coordinate RE^{3+} [30, 31]. Coordination competition is affected by not only the intrinsic coordination ability of the anion ligand but also the concentration of the ligand. As consequence of pH increment, the concentration of OH^- increases and the content and stability of CO_3^{2-} would also increase owing to right-hand shift of the $HCO_3^- \leftrightarrow CO_3^{2-} + H^+$ equilibrium. In view that the ability of inorganic anions to coordinate RE^{3+} generally follows the order $PO_4^{3-} > CO_3^{2-} > HPO_4^{2-} > SO_4^{2-} > OH^- > F^- > H_2PO_4^- > NCS^- > NO_3^- > Cl^- > ClO_4^-$ [30, 31], it can be concluded that gradually more OH^- and CO_3^{2-} and meanwhile less SO_4^{2-} (lower SO_4^{2-}/RE^{3+} molar ratio) would be incorporated into the amorphous precipitate with increasing solution pH, which is in compliance with the above experimental results of XRD. The crystallization of REOCSH (pH

= 6, 7) from an amorphous mass would proceed via a typical dissolution-reprecipitation (DR) process, which is very similar to the widely studied $CaCO_3$ system [32, 33]. However, the driving force for the dissolution of the initial amorphous mass would be controlled by the nucleation and growth of crystalline REOCSH [34-36]. Since part of the reactant solutes were fixed in the amorphous mass, the part of the solutes remaining in solution would thus dominate the thermodynamics and kinetics of REOCSH crystallization, and the greater the composition difference between the initial amorphous mass and REOCSH the more difficult it is for REOCSH to nucleate and grow. Owing to the small compositional deviation, the amorphous masses precipitated under pH = 6 and 7 underwent a complete DR process during hydrothermal treatment and thus REOCSH was crystallized as a pure phase. Another factor that may significantly affect the kinetics of DR is the solubility product (K_{sp}) of the initial mass. It is known that, owing to thermodynamic reason, the mass formed under a specific condition of chemical precipitation would have the lowest K_{sp} under equilibrium and K_{sp} varies with the condition of reaction. In view that the amorphous masses before hydrothermal reaction are essentially hydroxides, it can be inferred that their K_{sp} would decrease with increasing solution pH. The lower K_{sp} values of the pH = 8 and 10 ones may then make the DR process more difficult to occur through limiting the kinetics of solute exchange and, therefore, amorphous products were resulted even after the hydrothermal treatment. The microspheres shown in Fig. 2b,c were apparently formed via a typical aggregation mechanism [37], and the tending to be face-to-face alignment of the nanoflakes (the inset of Fig 2b) is the most efficient way to minimize the total surface energy of the system. It can also be inferred from the aggregation phenomena that the isoelectric point (E_{iso}) of the precipitates is around 7-8 (closer to 8). The

REOCSH nanoflakes would have positively charged surfaces under pH = 6, which hinders them from aggregation by electric repulsion, and thus discrete nanoflakes were produced (Fig. 2a). Similarly, the pH = 10 product was not formed as spherical aggregates, since the surfaces of the primary particles would be negatively charged under this pH value even though smaller particles have a stronger tendency to undergo aggregation.

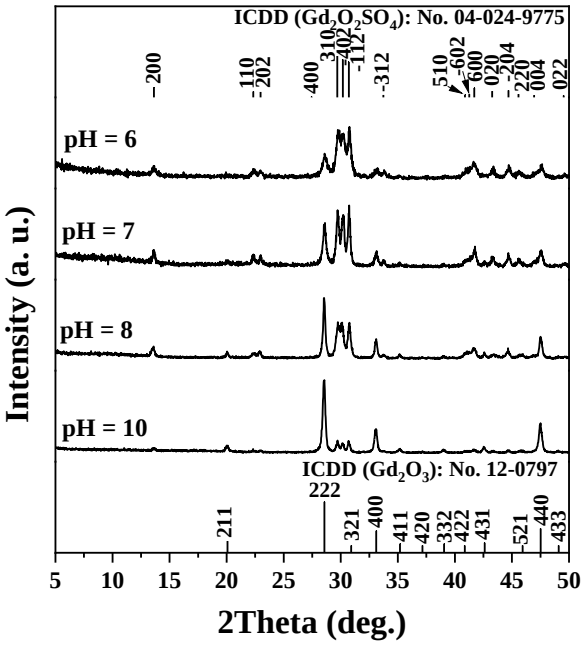

Fig. 4. XRD patterns of the products obtained by 800 °C calcination of the initial amorphous masses formed under different pH values.

Since thermal field is crucial for the nucleation and growth of the reprecipitated phase, we comparatively investigated the effect of hydrothermal temperature on the crystallization of REOCSH under pH = 6 and 7. XRD analysis (Fig. 5) found that no matter the pH value is 6 or 7, the products obtained at 100-180 °C all exhibited the characteristic diffractions of REOCSH, and diffraction intensity tends to increase with increasing reaction temperature. Noteworthy is that, at each temperatutre, the product of pH = 7 showed a lower diffraction intensity and more noisy diffraction peaks than its pH = 6 counterpart. This indicates a higher crystallization degree of the pH = 6 product, and can be understood by considering that the K_{sp} under pH = 6 is larger

than that under pH = 7, which facilitates the DR process. When the hydrothermal temperature reached 200 °C, monoclinic structured $RE(OH)SO_4$ (ICDD No. 18-2413) [8] appeared as an impurity phase under either pH = 6 or 7 (Fig. 5). Previous study on the $La(NO_3)_3$-$(NH_4)_2SO_4$-$NH_3{\cdot}H_2O$ hydrothermal system showed that the product would transform from layer-structured $La_2(OH)_4SO_4{\cdot}2H_2O$ (SO_4^{2-}-LLaH) into layer-structured $La(OH)SO_4$ when the temperature reached ~150 °C. The much higher temperature of $RE(OH)SO_4$ formation in this work could possibly be due to the different RE elements, in view of lanthanide contraction, and the interference of CO_3^{2-} anions. The appearance of $RE(OH)SO_4$ indicates phase separation and a lower content of CO_3^{2-} in the final product. This occurred owing to right-hand shift of the CO_3^{2-} ↔ HCO_3^- ↔ CO_2(g) equilibrium, since the solubility of CO_2 in water would decrease with increasing temperature, particularly under the slightly acidic/neutral conditions of pH = 6-7. FE-SEM analysis found that both the 100 and 120 °C products of pH = 7 contained amorphous nanoparticles (the insets in Fig. 6a,b), similar to those shown in Fig. S4, and the amorphous content of the former was significantly higher than that of the latter since REOCSH nanoflakes were more readily found in the 120 °C product (the inset in Fig. 6b). This indicates that the DR process was not complete below 140 °C. It is also clearly seen from the FE-SEM images (Fig. 6a-c) that microspheres were formed via coagulation of nano-sized primary particles, and a higher reaction temperature promotes the coagulated cluster to approach an ideal spherical shape. Additionally, the 180 °C product (average particle size ~21 μm; Fig. 6c) has an morphology almost identical to that observed from the 140 °C one (Fig. 2b). At the highest tested temperature of 200 °C, some of the microspheres were disintegrated owing to the formation of giant $RE(OH)SO_4$ plates (Fig. 6d). The above results thus indicate that pure

REOCSH is availble in the temperature range of ~140-180 °C under pH = 7. Under pH = 6, on the other hand, the 100 °C product (Fig. 6e) has already been REOCSH nanoplates and no amorphous particles were observed, indicating a much faster DR process owing to the larger K_{sp} at pH = 6 and the smaller compositional difference between the initial amorphous mass and REOCSH as discussed earlier for the results of XRD analysis (Fig. 5). The nanoplates have a better defined 2D morphology and straighter edges at a higher reaction temperature up to 180 °C, owing to a gradually higher degree of crystallization. Nanoplates should be the intrinsic morphology of REOCSH, since the compound has a layered structure in the tetragonal system and its (001) plane has the lowest surface energy [38, 39], which makes crystal growth along the [001] direction the hardest to proceed according to the Wulff theorem. The 200 °C product (Fig. 6h) consists of nanoplates (REOCSH) and giant plates ($RE(OH)SO_4$), comforming to a mixtutre of the two phases (Fig. 5b). Giant laths with a side length of ~100 μm were also observed for the hydrothermall synthesized $La(OH)SO_4$ and $Ce(OH)SO_4$ compounds [8, 40].

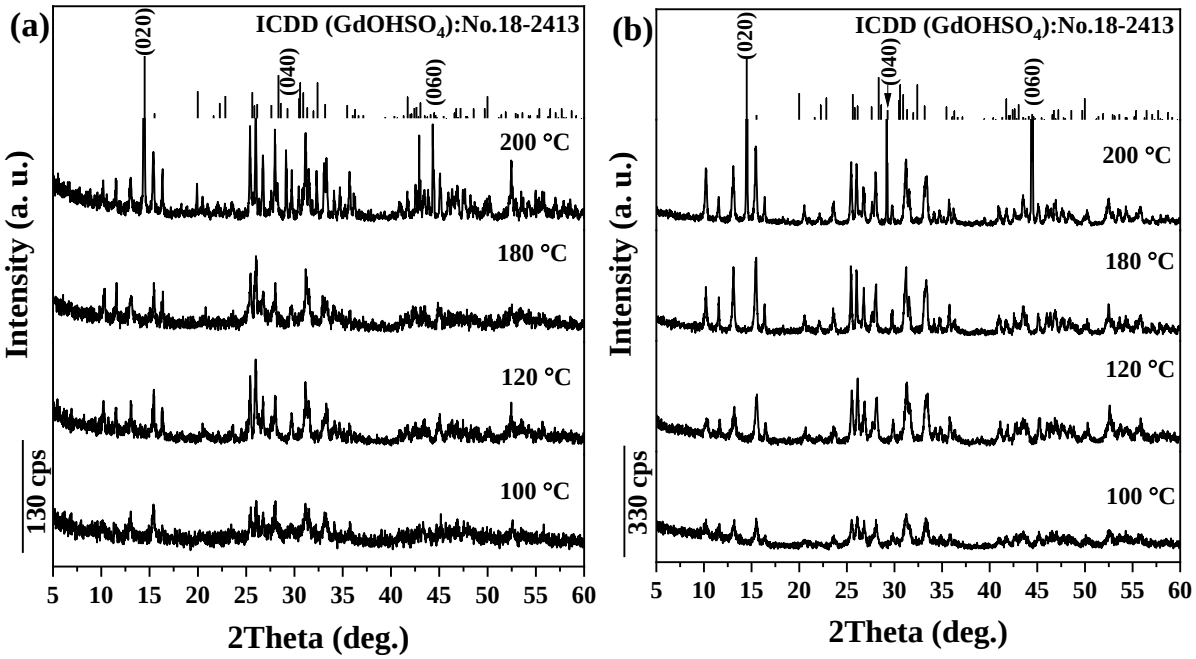

Fig. 5. XRD patterns of the products obtained at different temperatures under pH = 7 (a) and pH = 6 (b).

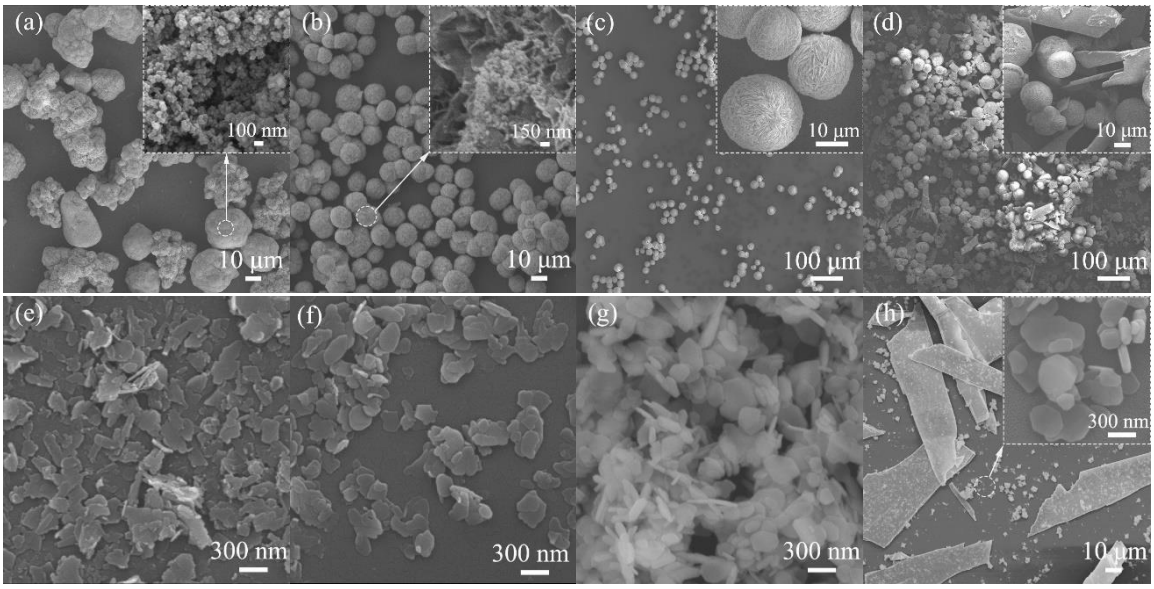

Fig. 6. FE-SEM morphologies of the products obtained at 100 °C (a, e), 120 °C (b, f), 180 °C (c, g) and 200 °C (d, h) under pH = 7 (a-d) and pH = 6 (e-h). The insets are closer views.

To further clarify the effect of solution pH on DR and morphology development, we tracked the time-course morphology evolution by FE-SEM for the products produced by 140 °C of hydrothermal reaction. It is seen from the results obtained under pH = 6 that the 30 min product (Fig. 7a) still maintained the morphology of the initial amorphous nanoparticles (Fig. S4) but a large number underdeveloped REOCSH nanoplates can be observed in the 1 h product (Fig. 7b), and the 3 h product contained only REOCSH nanoplates (Fig. 7c). The results indicate a quite fast phase conversion via DR under pH = 6 and, again, this is due to the relative large K_{sp} and the small compositional deviation between the initial amorphous mass and REOCSH. Fig. 7d-g show the results obtained under pH = 7, where it is seen that the 30 min product consists of amorphous nanoparticles (Fig. 7d). After 1 h of reaction, in addition to amorphous nanoparticles, a small amount of spherical particles (colloid spheres) with a diameter of ~1 μm and smooth surfaces were observed in the product (Fig. 7e and the inset). This indicates the commencement of nanoparticle aggregation. Observation of the 3 h product (Fig. 7f) found ~10 μm-sized microspheres embedded in a matrix mass, and closer view showed that the

microsphere contains both nanoparticles and nanoplates (the left-hand inset in Fig. 7f) and the matrix consists of nanoparticles and ~1 μm-sized colloid spheres (the right-hand inset in Fig. 7f). After reaction for 6 h (Fig. 7g), the portion of microspheres increased dramatically, which was accompanied by vanishing of the matrix mass. Besides, closer observation (the inset in Fig. 7g) showed that the microspheres formed after 6 h of reaction has much fewer nanoparticles (Fig. 7g) than those formed after 3 h of reaction (the left-hand inset in Fig. 7f) due to more crystallization of the REOCSH phase. The above observations indicated that, under pH = 7, the crystallization of REOCSH started at ~3 h of reaction at 140 °C and that the ~10 μm-sized microspheres were formed via growth of the ~1 μm-sized colloid spheres. The observed evolution of flaky REOCSH crystallites is in accordance with the results of phase analysis via XRD (Fig. S5), and the course of microsphere formation is schematically shown in Fig. 7h.

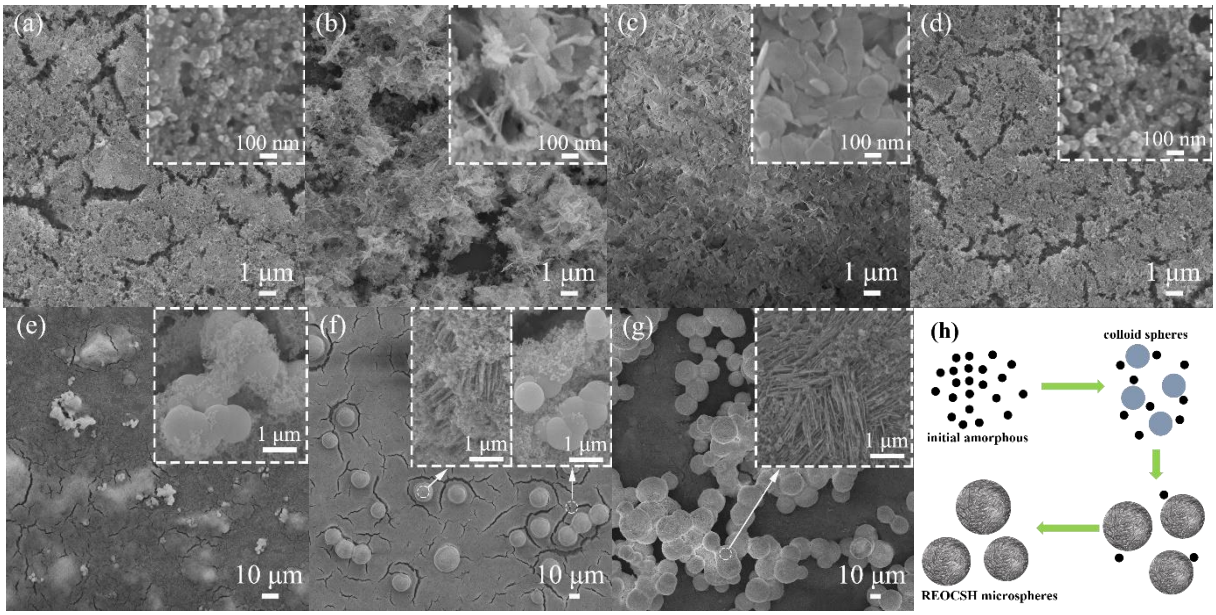

Fig. 7. FE-SEM morphologies of the products obtained by hydrothermal reaction under pH = 6 (a-c) and pH = 7 (d-g) for 30 min (a, d), 1 h (b, e), 3 h (c, f) and 6 h (g). The insets are closer views and part (h) is a schematic illustration of the growth mechanism of microspheres under pH = 7.

3.2 Derivation and characterization of $RE_2O_2SO_4$

REOCSH has the same RE/S molar ratio of $RE_2O_2SO_4$, so it can be used as a precursor to derive $RE_2O_2SO_4$ by proper calcination without the emission of harmful SO_x gases. Our

previous study via differential thermal analysis/thermogravimetry (DTA/TG, heating rate 10 °C/min) showed that GdOCSH would decompose into $Gd_2O_2SO_4$ in air via dehydroxylation and decarbonation up to 800 °C ($Gd_2(OH)_2CO_3SO_4 \cdot nH_2O \rightarrow Gd_2O_2SO_4 + CO_2 + (n + 1)H_2O$) , followed by further decomposition into Gd_2O_3 when the temperature is over ~1000 °C ($Gd_2O_2SO_4 \rightarrow Gd_2O_3 + SO_3$). We thus selected 800 °C as a proper temperature to derive $RE_2O_2SO_4$ (RE = $Gd_{0.95}Eu_{0.05}$) from the REOCSH precursors formed via hydrothermal reaction at 140 °C and pH = 6 and 7. Fig. 8a shows the XRD patterns of the calcination products, where it is seen that phase-pure $RE_2O_2SO_4$ was obtained in each case since all the diffraction peaks can be well indexed with those of the $Gd_2O_2SO_4$ (monoclinic, space group *C*2/*c*; ICDD No. 04-024-9775). Broadening analysis of the XRD peaks with Scherrer formula [41] found that the $RE_2O_2SO_4$ powders from the pH = 6 and 7 precursors have average crystallite sizes of ~24 and 27 nm, respectively. Analysis of the XRD patterns with the Jade 6 software found that both the $RE_2O_2SO_4$ powders have the similar lattice parameters of a ~ 13.6204(2) Å, b ~ 4.1769(4) Å and c ~ 8.1223(3) Å, cell volume V of 441.39(5) Å^3, and axis angle β of 107.21(4)°. The cell volume is slightly larger than that of pure $Gd_2O_2SO_4$ (V = 439.82 Å^3; ICDD No. 04-024-9775) due to the incorporation of 5 at.% of larger Eu^{3+} ions (1.12 Å for Eu^{3+} and 1.107 Å for Gd^{3+} under coordination number CN = 9) and indicates the formation of $(Gd,Eu)_2O_2SO_4$ solid solution. FE-SEM observation indicated that the microspheres of REOCSH (Fig. 8b) essentially maintained their original shapes after 800 °C calcination though cracking occurred due to the stress arising from mass loss (release of H_2O and CO_2) and intra-sphere sintering. The $RE_2O_2SO_4$ powder calcined from the REOSCH nanoplates (Fig. 8c) tends to have a nanoplate-like particle morphology, though the original platelets became porous and tend to disintegrate by the mass loss during calcination.

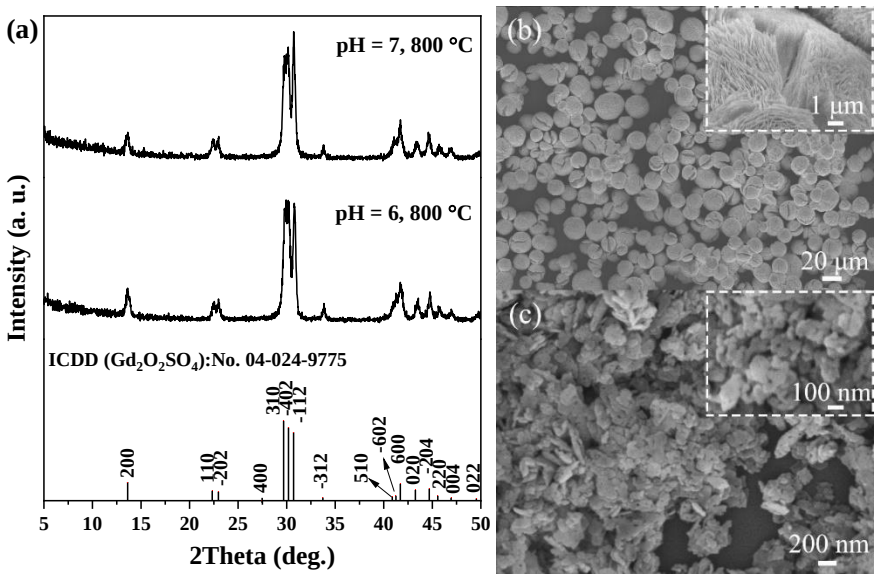

Fig. 8. XRD patterns of the products calcined in air at 800 °C (a), and parts (b) and (c) respectively show FE-SEM morphologies of the $RE_2O_2SO_4$ calcined from REOCSH microspheres and nanoplates.

3.3 Photoluminescence properties of the $(Gd_{0.95}Eu_{0.05})_2O_2SO_4$ phosphors

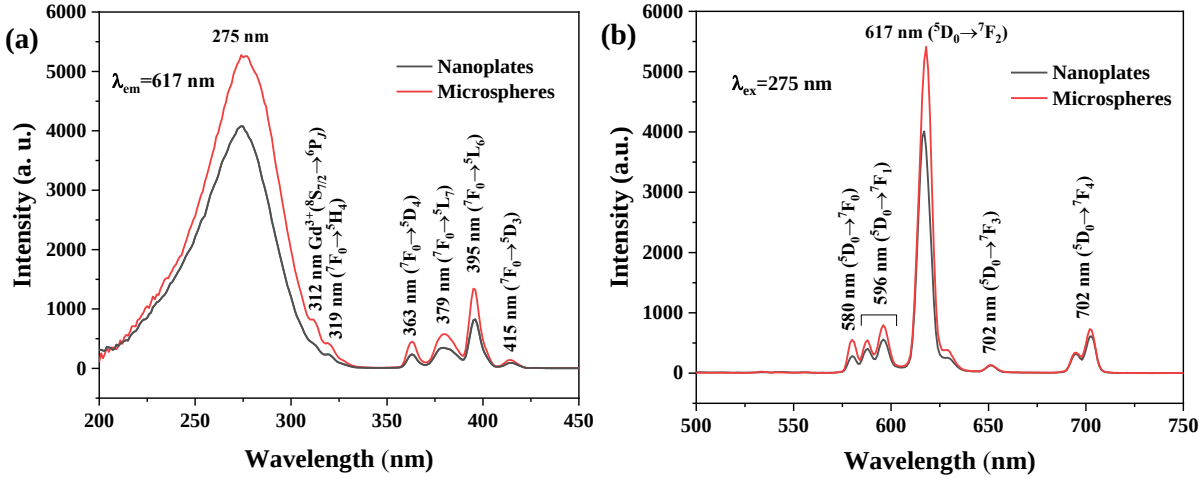

Fig. 9. PLE (a) and PL (b) spectra of the $(Gd,Eu)_2O_2SO_4$ phosphors shown in Fig. 8b (microspheres) and Fig. 8c (nanoplates).

Fig. 9 shows the excitation (PLE) and emission (PL) spectra of the two kinds of $(Gd,Eu)_2O_2SO_4$ phosphor powders. It is seen that both the nanoplates and microspheres share similar spectral profiles. The PLE spectra (Fig. 9a), taken by monitoring the red emission of Eu^{3+} at 617 nm, contain a broad and strong band centered at ~275 nm and a few weak and sharp peaks in the longer wavelength region in each case. The broad band largely originates from O^{2-}-Eu^{3+} charge transfer (CT, excitation of electrons from the 2*p* orbital of O to the 4*f* orbital

of Eu) [42], which is overlapped with the $^8S_{7/2} \rightarrow {}^6I_J$ (~275 nm) and $^8S_{7/2} \rightarrow {}^6P_J$ (~312 nm) intra-4f^7 excitation transition of Gd^{3+} [43, 44], while the sharp peaks correspond to intra-4f^6 transitions of Eu^{3+} as labelled in the figure. Under excitation with the peak wavelength of the CT band (275 nm), both the $(Gd,Eu)_2O_2SO_4$ phosphors exhibited the typical $^5D_0 \rightarrow {}^7F_J$ (J = 0-4) emissions of Eu^{3+}, with the $^5D_0 \rightarrow {}^7F_2$ red one (~617 nm) being the most prominent (Fig. 9b). Noteworthy is that the 617 nm emission of the microspheres is ~1.35 times as strong as that of the nanoplates, since the microspheres have a much larger particle size and the spherical particle shape reduced surface scattering of the excitation light (stronger excitation absorption, Fig. S6). Analysis of the PL spectra with the built-in software of the spectrophotometer found that the microspheres and nanoplates have quantum efficiencies of ~40.8% and 32.1%, respectively. Analyzing the fluorescence decay curves with equation $I = A\exp(-t/\tau) + B$, where τ is fluorescence lifetime, t is delay time, I is emission intensity and A and B are constants, found that the 617 nm main emission (λ_{em} = 617 nm, λ_{ex} = 275 nm) decayed in a single exponential manner (Fig. 10a) and that the microspheres and nanoplates have τ values of ~1.32 and 2.43 ms, respectively. Though the lifetimes fall in the range of 0.71-4.37 ms reported for the red emission of Eu^{3+} in some oxide/oxysulfide hosts [45-48], the obviously longer lifetime of the nanoplates could be due to smaller particle size. It is known that τ can be correlated with the effective refractive index of the material (n_{eff}) via equation $\tau \sim [(\lambda_0^2/f(\mathrm{ED})]/[n_{eff}(n_{eff}^2+2)^2]$, where f(ED) is the oscillator strength for electric dipole transition and λ_0 is the wavelength in vacuum [49]. The n_{eff} in the equation can be further expressed as $n_{eff} = x \cdot n_c + (1-x) \cdot n_{med}$, where x is the filling factor, that is, the fraction of space occupied by the particle in the surrounding medium (air in this work), and n_c and n_{med} are the refractive indices of the bulk material and the surrounding medium, respectively. n_{eff} roughly equals to n_{med} for extremely small particles,

since the *x* value approaches 0. For the intermediately sized particles of this work, n_{eff} is affected by particle size and decreases for smaller particles. This may account for the longer fluorescence lifetime of the $(Gd,Eu)_2O_2SO_4$ nanoplates, since they are much smaller than the microspheres. Despite the different particle morphologies, both the types of $(Gd,Eu)_2O_2SO_4$ phosphors have almost the same Internationale de L'Eclairage (CIE) chromaticity coordinates of around (0.653, 0.345), typical of a red color (Fig. 10b).

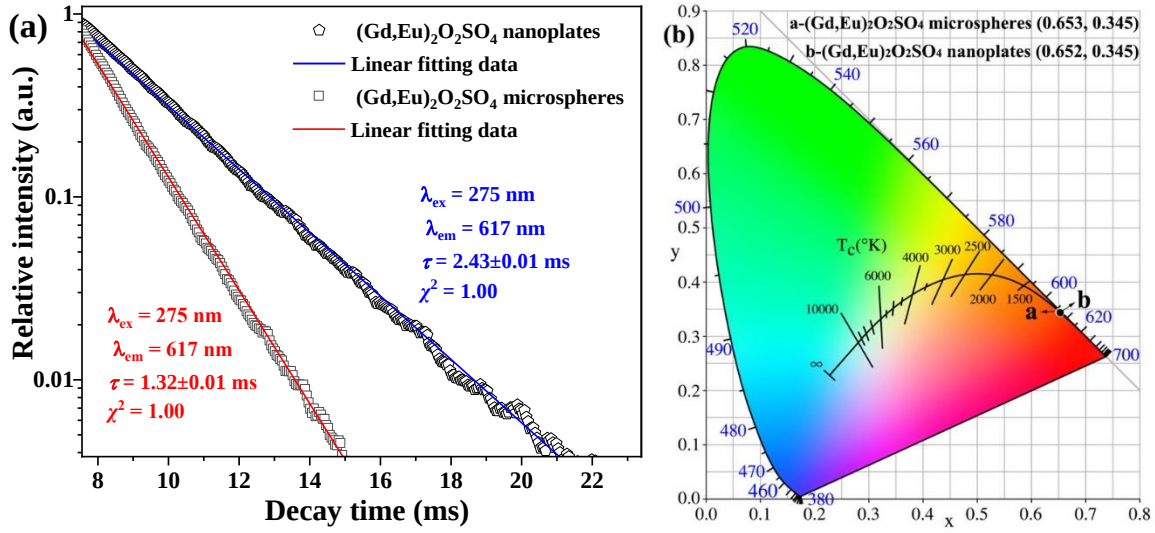

Fig. 10. Fluorescence decay behaviors of the 617 nm emission (a) and a CIE chromaticity diagram (b) for the two types of $(Gd,Eu)_2O_2SO_4$ phosphors.

To evaluate the thermal stability of luminescence, temperature-dependent PL spectra were taken for the microspheres under 275 nm excitation. It is seen from the results displayed in Fig. 11a that raising the measurement temperature up to 300 °C did not produce new emission and did not appreciably alter the position of the existing emission peaks, but successively weakened the luminescence of Eu^{3+} due to thermal quenching. It is seen from the normalized intensity (Fig. 11b) that the 617 nm emission retained ~81% and 53% of its room-temperature (RT) intensity at 150 and 300 °C, respectively, showing a good thermal stability of luminescence. The value at 150 °C, a temperature frequently used to evaluate whether a phosphor is suitable for high-power LED application, is higher than that of Y_2O_2S:Eu (42.8%) [50] and is almost

the same as that of Y_2O_3:Eu (82%) [51]. The activation energy (E_a) of thermal quenching can be derived with the Arrhenius equation [52]:

$$I = \frac{I_0}{1 + cexp(\frac{-E_a}{kT})} \quad (1)$$

where I_0 and I are the initial emission intensity and the emission intensity at a given temperature T (in Kelvin), respectively, c is a pre-exponential constant, and k is Boltzmann constant (8.617×10^{-5} eV). $\ln[(I_0/I\text{-}1)]$ *vs* $1/(kT)$ transformation of the experimental data for the measured temperature range of 323-573 K displayed a nearly straight line (the inset in Fig. 11b), and linear fitting yielded an E_a value of ~0.19±0.01 eV. It is seen from Table S1 that the color coordinates of Eu^{3+} luminescence slightly drifted from (0.653, 0.345) to (0635, 0.361) with increasing temperature from 25 to 300 °C, corresponding to color changes toward the orange red region of the CIE chromaticity diagram (Fig. S7). The extent of chromaticity shift (ΔE) can be evaluated by applying the equation [53]:

$$\Delta E = \sqrt{(u'_f - u'_i)^2 + (v'_f - v'_i)^2 + (w'_f - w'_i)^2} \quad (2)$$

where $u' = 4x/(3\text{-}2x\text{+}12y)$, $v' = 9y/(3\text{-}2x\text{+}12y)$ and $w' = 1\text{-}\ u'\text{-}\ v'$, x and y are the CIE coordinates, and f and i refer to the measurement temperature and initial temperature (25 °C), respectively. The results of calculation (Table S1) indicated that ΔE gradually increased with increasing temperature, which is ~0.9% at 150 °C and ~3.8% at 300 °C. The continuous color drift (Fig. S7) implies a gradually stronger emission of lights shorter than 617 nm. We thus examined the intensity variations of the $^5D_{0,1} \rightarrow {}^7F_{0,1,2}$ transitions. Taking 617, 596, 580, 556 and 533 nm as the typical emission wavelengths of $^5D_0 \rightarrow {}^7F_2$ (Fig. 9b), $^5D_0 \rightarrow {}^7F_1$ (Fig. 9b), $^5D_0 \rightarrow {}^7F_0$ (Fig. 9b), $^5D_1 \rightarrow {}^7F_2$ (Fig. S8) and $^5D_1 \rightarrow {}^7F_1$ (Fig. S8), respectively, it was found that the I_{617}/I_{596} and I_{617}/I_{580} intensity ratios only slightly decreased while the I_{617}/I_{556} and I_{617}/I_{533} ones were

dramatically reduced with increasing temperature up to 300 °C (Table S1). This clearly indicates that the color drift of luminescence was mainly caused by gradually stronger emissions from the $^5D_1$ level, which can be understood by considering that the $^5D_1/^5D_0$ energy levels of Eu^{3+} are thermally coupled and, therefore, the excited electrons at $^5D_0$ can be promoted to the higher lying $^5D_1$ level by thermal activation.

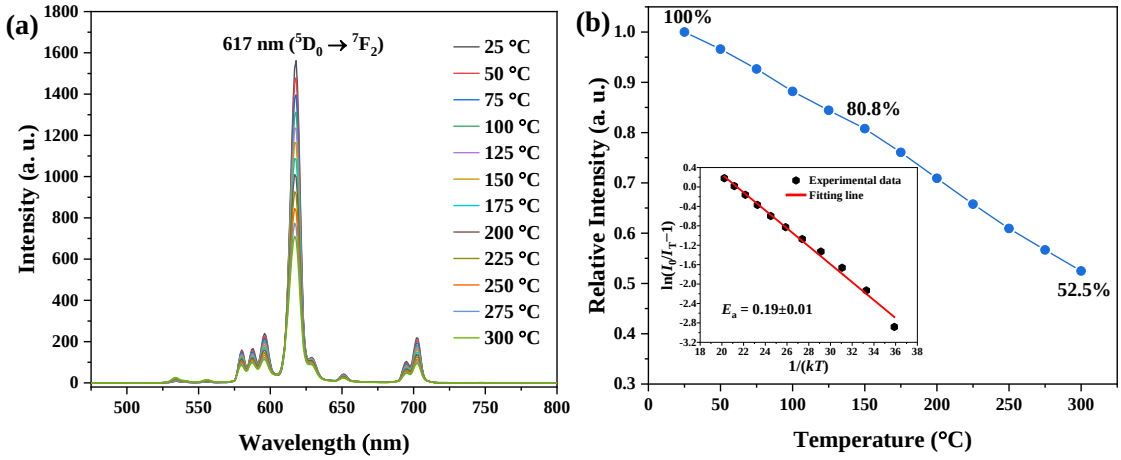

Fig. 11. Temperature-dependent PL spectra (a) and relative intensity of the 617 nm emission as a function of the measurement temperature (b) for the $(Gd,Eu)_2O_2SO_4$ microspheres under 275 nm excitation. The inset in (b) is the $\ln(I_0/I_T - 1)$ *versus* $1/(kT)$ plot for determination of the activation energy for thermal quenching of luminescence.

4. Conclusion

$RE_2(OH)_2CO_3SO_4{\cdot}nH_2O$ layered compound (RE = $Gd_{0.95}Eu_{0.05}$, REOCSH) was obtained via hydrothermal reaction at 140 °C for 24 h, and its particle morphology was successfully regulated from microsphere (~25 μm in diameter) to nanoplate (~400 nm in length) by adjusting the solution pH from 7 to 6. Solution pH substantially affected the chemical composition and crystallization kinetics of the initial amorphous precipitate and, therefore, influenced the crystallization of REOCSH via dissolution-reprecipitation during hydrothermal treatment. Investigation of the temperature-course and time-course of phase/morphology evolution showed that the microspheres were formed via a typical aggregation process under pH = 7.

Calcining the two types of REOCSH in air at 800 °C produced $(Gd_{0.95}Eu_{0.05})_2O_2SO_4$ monospheres and nanoplates, and the former showed a luminescence intensity ~1.35 times that of the latter (λ_{ex} = 275 nm, λ_{em} = 617 nm). The 617 nm red emission of Eu^{3+} in the monospheres has a lifetime of ~1.32 ms and retained ~81% of its room temperature intensity at 150 °C (activation energy of thermal quenching ~0.19 eV). Despite the different particle morphologies, both the types of $(Gd,Eu)_2O_2SO_4$ have chromaticity coordinates of around (0.653, 0.345) for their luminescence at room temperature. A gradual chromaticity drift was observed for the luminesce of the monospheres up to the highest measurement temperature of 300 °C, which was analyzed to be largely due to stronger emissions from the $^5D_1$ level of Eu^{3+}.

Acknowledgements

This work was supported in part by the National Natural Science Foundation of China (Grant No. 52172112 and 51972047).

References

[1] M. Machida, K. Kawamura, K. Ito, K. Ikeue, Large-capacity oxygen storage by lanthanide oxysulfate/oxysulfide systems, Chem. Mater., 17 (2005) 1487-1492.
[2] K. Ikeue, M. Eto, D. Zhang, T. Kawano, M. Machida, Large-capacity oxygen storage of Pd-loaded $Pr_2O_2SO_4$ applied to anaerobic catalytic CO oxidation, J. Catal., 248 (2007) 46-52.
[3] A. Kasten, G. Hess, Magnetic Properties of $Tb_2O_2SO_4$, Phys. Status Solidi B, 123 (1984) 123-134.
[4] H. Hülsing, H.G. Kahle, M. Schwab, H.J. Schwarzbauer, Specific heat of rare earth oxisulphates ($RE_2O_2SO_4$), J. Magn. Magn. Mater., 9 (1978) 68-70.
[5] W. Paul, Magnetism and magnetic phase diagram of $Gd_2O_2SO_4$ I. Experiments, J. Magn. Magn. Mater., 87 (1990) 23-28.
[6] G. Chen, F. Chen, X. Liu, W. Ma, H. Luo, J. Li, R. Ma, G. Qiu, Hollow spherical rare-earth-doped yttrium oxysulfate: A novel structure for upconversion, Nano Res., 7 (2014) 1093-1102.
[7] L. Song, P. Du, Q. Jiang, H. Cao, J. Xiong, Synthesis and luminescence of high-brightness $Gd_2O_2SO_4:Tb^{3+}$ nanopieces and the enhanced luminescence by alkali metal ions co-doping, J. Lumin., 150 (2014) 50-54.
[8] X. Wang, J.-G. Li, M.S. Molokeev, Q. Zhu, X. Li, X. Sun, Layered hydroxyl sulfate: Controlled crystallization, structure analysis, and green derivation of multi-color luminescent

$(La,RE)_2O_2SO_4$ and $(La,RE)_2O_2S$ phosphors (RE = Pr, Sm, Eu, Tb, and Dy), Chem. Eng. J., 302 (2016) 577-586.
[9] Y. Zhou, F. Li, X. Wang, Q. Zhu, X. Li, X. Sun, J.-G. Li, Facile synthesis of $Gd_2O_2SO_4$:Tb and Gd_2O_2S:Tb green phosphor nanopowders of unimodal size distribution and photoluminescence, Adv. Powder Technol., 32 (2021) 1911-1919.
[10] S. Zhukov, A. Yatsenko, V. Chernyshev, V. Trunov, E. Tserkovnaya, O. Antson, J. Hölsä, P. Baulés, H. Schenk, Structural study of lanthanum oxysulfate $(LaO)_2SO_4$, Mater. Res. Bull., 32 (1997) 43-50.
[11] O. Siidra, D. Charkin, I. Plokhikh, E. Nazarchuk, A. Holzheid, G. Akimov, Expanding family of litharge-derived sulfate minerals and synthetic compounds: Preparation and crystal structures of $[Bi_2CuO_3]SO_4$ and $[Ln_2O_2]SO_4$ (Ln = Dy and Ho), Miner., 10 (2020) 887.
[12] C.B. Murray, C.R. Kagan, M.G. Bawendi, Self-organization of CdSe nanocrystallites into three-dimensional quantum dot superlattices, Science, 270 (1995) 1335-1338.
[13] G. Wu, H. Qin, S. Feng, X. Tan, Z. Luo, Y. Liu, H. Shao, J. Jiang, H. Jiang, Ultrafine Gd_2O_2S:Pr powders prepared via urea precipitation method using SO_2/SO_4^{2-} as sulfuration agent—A comparative study, Powder Technol., 305 (2017) 382-388.
[14] H. Qin, X. Tan, W. Huang, J. Jiang, H. Jiang, Application of urea precipitation method in preparation of advanced ceramic powders, Ceram. Int., 41 (2015) 11598-11604.
[15] Y. Xia, P. Yang, Y. Sun, Y. Wu, B. Mayers, B. Gates, Y. Yin, F. Kim, H. Yan, One-dimensional nanostructures: Synthesis, characterization, and applications, Adv. Mater., 15 (2003) 353-389.
[16] X. Wang, J. Zhuang, Q. Peng, Y. Li, A general strategy for nanocrystal synthesis, Nature, 437 (2005) 121-124.
[17] M. Wang, Y. Tang, T. Sun, G. Jiang, Y. Shi, Yolk–shell $ZnWO_4$ microspheres: one-pot synthesis, characterization and photocatalytic properties, CrystEngComm, 16 (2014) 11035-11041.
[18] M. Li, X. Wang, Q. Zhu, J.-G. Li, B.-N. Kim, Crystallization and architecture engineering of $ZnWO_4$ for enhanced photoluminescence, CrystEngComm, 22 (2020) 6398-6406.
[19] S.w. Kim, T. Masui, N. Imanaka, Synthesis of red-emitting phosphors based on gadolinium oxysulfate by a flux method, Electrochemistry, 77 (2009) 611-613.
[20] M. Machida, K. Kawamura, T. Kawano, D. Zhang, K. Ikeue, Layered Pr-dodecyl sulfate mesophases as precursors of $Pr_2O_2SO_4$ having a large oxygen-storage capacity, J. Mater. Chem., 16 (2006) 3084-3090.
[21] D. Zhang, F. Yoshioka, K. Ikeue, M. Machida, Synthesis and oxygen release/storage properties of Ce-substituted La-oxysulfates, $(La_{1-x}Ce_x)_2O_2SO_4$, Chem. Mater., 20 (2008) 6697-6703.
[22] M. Yang, H. Shi, L. Ma, Q. Gui, J. Ma, M. Lin, A. Sunna, W. Zhang, L. Dai, J. Qu, Y. Liu, Multifunctional luminescent nanofibres from Eu^{3+}-doped $La_2O_2SO_4$ with enhanced oxygen storage capability, J. Alloys Compd., 695 (2017) 202-207.
[23] J. Liang, R. Ma, F. Geng, Y. Ebina, T. Sasaki, $Ln_2(OH)_4SO_4 \cdot nH_2O$ (Ln = Pr to Tb; $n \sim 2$): A new family of layered rare-earth hydroxides rigidly pillared by sulfate ions, Chem. Mater., 22 (2010) 6001-6007.
[24] X. Wang, J.-G. Li, M.S. Molokeev, X. Wang, W. Liu, Q. Zhu, H. Tanaka, K. Suzuta, B.-N. Kim, Y. Sakka, Hydrothermal crystallization of a $Ln_2(OH)_4SO_4 \cdot nH_2O$ layered compound

for a wide range of Ln (Ln = La–Dy), thermolysis, and facile transformation into oxysulfate and oxysulfide phosphors, RSC Adv., 7 (2017) 13331-13339.
[25] X. Wang, M.S. Molokeev, Q. Zhu, J.-G. Li, Controlled hydrothermal crystallization of anhydrous $Ln_2(OH)_4SO_4$ (Ln=Eu–Lu, Y) as a new family of layered rare earth metal hydroxides, Chem. Eur. J., 23 (2017) 16034-16043.
[26] X. Wang, J.-G. Li, Q. Zhu, X. Sun, Photoluminescence of $(La,Eu)_2O_2SO_4$ red-emitting phosphors derived from layered hydroxide, J. Mater. Res., 31 (2016) 2268-2276.
[27] F. Li, M. Jin, Z. Li, X. Wang, Q. Zhu, J.-G. Li, Vertically aligned $Gd_2O_2SO_4$:Ln and Gd_2O_2S:Ln luminescent films with super-hydrophobicity via a novel precursor route (Ln = Pr, Eu, Tb), Appl. Surf. Sci., 609 (2023) 155323.
[28] J.A. Gadsden, Infrared spectra of minerals and related inorganic compounds, Butterworth, London, 1975.
[29] Y.G. Denisenko, A.E. Sedykh, S.A. Basova, V.V. Atuchin, M.S. Molokeev, A.S. Aleksandrovsky, A.S. Krylov, A.S. Oreshonkov, N.A. Khritokhin, E.I. Sal'nikova, O.V. Andreev, K. Müller-Buschbaum, Exploration of the structural, spectroscopic and thermal properties of double sulfate monohydrate $NaSm(SO_4)_2 \cdot H_2O$ and its thermal decomposition product $NaSm(SO_4)_2$, Adv. Powder Technol., 32 (2021) 3943-3953.
[30] R.L. Rich, Inorganic reactions in water, Springer-Verlag, Berlin Heidelberg, 2007.
[31] M. Li, J.-G. Li, Extensive tailoring of $REPO_4$ and $REVO_4$ crystallites via solution processing and luminescence, CrystEngComm, 24 (2022) 4841-4852.
[32] J.-P. Andreassen, Formation mechanism and morphology in precipitation of vaterite—nano-aggregation or crystal growth?, J. Cryst. Growth, 274 (2005) 256-264.
[33] Z. Liu, Z. Zhang, Z. Wang, B. Jin, D. Li, J. Tao, R. Tang, J.J. De Yoreo, Shape-preserving amorphous-to-crystalline transformation of $CaCO_3$ revealed by in situ TEM, Proc. Natl. Acad. Sci. U. S. A., 117 (2020) 3397-3404.
[34] L. Hu, R. Ma, T.C. Ozawa, T. Sasaki, Synthesis of a solid solution series of layered $Eu_xGd_{1-x}(OH)_{2.5}Cl_{0.5} \cdot 0.9H_2O$ and its transformation into $(Eu_xGd_{1-x})_2O_3$ with enhanced photoluminescence properties, Inorg. Chem., 49 (2010) 2960-2968.
[35] L. Hu, R. Ma, T.C. Ozawa, F. Geng, N. Iyi, T. Sasaki, Oriented films of layered rare-earth hydroxide crystallites self-assembled at the hexane/water interface, Chem. Commun., (2008) 4897-4899.
[36] Q. Zhu, J.-G. Li, C. Zhi, R. Ma, T. Sasaki, J.X. Xu, C.H. Liu, X.D. Li, X.D. Sun, Y. Sakka, Nanometer-thin layered hydroxide platelets of $(Y_{0.95}Eu_{0.05})_2(OH)_5NO_3 \cdot xH_2O$: exfoliation-free synthesis, self-assembly, and the derivation of dense oriented oxide films of high transparency and greatly enhanced luminescence, J. Mater. Chem. C, 21 (2011) 6903-6908.
[37] J. Park, V. Privman, E. Matijević, Model of formation of monodispersed colloids, J. Phys. Chem. B, 105 (2001) 11630-11635.
[38] F. Geng, Y. Matsushita, R. Ma, H. Xin, M. Tanaka, F. Izumi, N. Iyi, T. Sasaki, General synthesis and structural evolution of a layered family of $Ln_8(OH)_{20}Cl_4 \cdot nH_2O$ (Ln = Nd, Sm, Eu, Gd, Tb, Dy, Ho, Er, Tm, and Y), J. Am. Chem. Soc., 130 (2008) 16344-16350.
[39] X. Wu, J.-G. Li, Q. Zhu, W. Liu, J. Li, X. Li, X. Sun, Y. Sakka, One-step freezing temperature crystallization of layered rare-earth hydroxide $(Ln_2(OH)_5NO_3 \cdot nH_2O)$ nanosheets for a wide spectrum of Ln (Ln = Pr-Er, and Y), anion exchange with fluorine and sulfate, and microscopic coordination probed via photoluminescence, J. Mater. Chem. C, 3 (2015) 3428-

3437.
[40] Z. Han, Y. Qian, J. Yang, G.Q. Lu, Soft solution processing of cerium hydroxysulfate powders with different morphologies, J. Mater. Chem., 13 (2003) 150-153.
[41] P. Scherrer, Estimation of the size and internal structure of colloidal particles by means of röntgen, Göttinger Nachrichten Math. Phys., 2 (1918) 96-100.
[42] Q. Cheng, M. Kang, J. Wang, P. Zhang, R. Sun, L. Song, Low temperature microwave solid-state synthesis of $CaCO_3$:Eu^{3+}, K^+ phosphors, Adv. Powder Technol., 26 (2015) 848-852.
[43] Y. Sun, H. Zou, B. Zhang, X. Zhou, Y. Song, K. Zheng, Z. Shi, Y. Sheng, Luminescent properties and energy transfer of Gd^{3+}/Eu^{3+} co-doped cubic $CaCO_3$, J. Lumin., 178 (2016) 307-313.
[44] J.-G. Li, X. Li, X. Sun, T. Ishigaki, Monodispersed colloidal spheres for uniform Y_2O_3:Eu^{3+} red-phosphor particles and greatly enhanced luminescence by simultaneous Gd^{3+} doping, J. Phys. Chem. C, 112 (2008) 11707-11716.
[45] Z. Wang, P. Wang, J. Zhong, H. Liang, J. Wang, Phase transformation and spectroscopic adjustment of Gd_2O_3:Eu^{3+} synthesized by hydrothermal method, J. Lumin., 152 (2014) 172-175.
[46] L. Li, P. Yang, W. Chang, X. Tang, C. Li, Z. Zeng, S. Jiang, X. Zhou, Multifunctional broad-band excited Eu^{3+}-activated fluorescent materials for potential warm white light-emitting diodes (w-LEDs) and temperature sensor applications, Adv. Powder Technol., 29 (2018) 43-49.
[47] X. Xu, B. Lu, J. Hu, Z. Sun, H. Chen, Controlled synthesis and photoluminescence behaviors of Lu_2O_3:Eu and Lu_2O_2S:Eu phosphor particles, J. Lumin., 215 (2019) 116702.
[48] B. Zhang, H. Zou, Y. Song, H. Guan, X. Zhou, Z. Shi, Y. Sheng, Electrospinning fabrication and luminescence properties of Lu_2O_2S:Eu^{3+}fibers, CrystEngComm, 19 (2016) 699-707.
[49] R.S. Meltzer, S.P. Feofilov, B. Tissue, H.B. Yuan, Dependence of fluorescence lifetimes of Y_2O_3:Eu^{3+} nanoparticles on the surrounding medium, Phys. Rev. B, 60 (1999) R14012-R14015.
[50] Z. Sun, G. Cao, Q. Zhang, Y. Li, H. Wang, Thermal stable Eu-doped $CaTiO_3$ phosphors with morphology-control for high-power tricolor white LEDs, Mater. Chem. Phys., 132 (2012) 937-942.
[51] A. Dwivedi, M. Srivastava, A. Dwivedi, A. Srivastava, A. Mishra, S.K. Srivastava, Synthesis and enhanced photoluminescence properties of red emitting divalent ion (Ca^{2+}) doped Eu:Y_2O_3 nanophosphors for optoelectronic applications, J. Rare Earths, 40 (2022) 1187-1198.
[52] X. Wang, X. Feng, C. Gong, M. Sun, C. Wang, Q. Wang, J.-G. Li, $(La,Dy)_2W_2O_9$ tungstates: Selected synthesis, enhanced luminescence through Gd^{3+} co-doping, and favorable quantum efficiency, Adv. Powder Technol., 33 (2022) 103392.
[53] X. Zhang, L. Huang, F. Pan, M. Wu, J. Wang, Y. Chen, Q. Su, Highly thermally stable single-component white-emitting silicate glass for organic-resin-free white-light-emitting diodes, ACS Appl. Mater. Interfaces, 6 (2014) 2709-2717.